Automated Global Classification of Surface Layer Stratification Using High-Resolution Sea Surface Roughness Measurements by Satellite Synthetic Aperture Radar

Justin E. Stopa[1] [iD], **Chen Wang[2]** [iD], **Doug Vandemark[3]** [iD], **Ralph Foster[4]**, **Alexis Mouche[5]** [iD], and **Bertrand Chapron[5]** [iD]

[1]Department of Ocean Resources and Engineering, School of Ocean and Earth Science and Technology, University of Hawai'i at Mānoa, Honolulu, HI, USA, [2]School of Marine Sciences, Nanjing University of Information Science and Technology, Nanjing, China, [3]Ocean Processes Analysis Laboratory, University of New Hampshire, Durham, NH, USA, [4]Applied Physics Laboratory, University of Washington, Seattle, WA, USA, [5]University Brest, CNRS, IRD, Ifremer, Laboratoire d'Océanographie Physique et Spatiale (LOPS), IUEM, Brest, France

Abstract A three-state global estimator of marine surface layer atmospheric stratification is demonstrated using more than 600,000 Sentinel-1 synthetic aperture radar wave mode images at incidence angle $\approx 36.8°$. Stratification is quantified using a bulk Richardson number, Ri, derived from collocated ERA5 surface analyses. The three stratification states are defined as unstable: $Ri < -0.012$, near-neutral: $-0.012 < Ri < +0.001$, and stable: $Ri > +0.001$. These boundaries are identified by the characteristic boundary layer coherent structures that form in these regimes and modulate the surface roughness imaged by the radar. An automated machine learning algorithm identifies the coherent structures impressed on the images. Data from 2016 to 2019 are used to examine spatial and temporal variation in these state estimates in terms of expected wind and thermal forcing. This new satellite-based approach for detecting air-sea stratification has implications for weather modeling and air-sea flux products.

Plain Language Summary The air-sea fluxes of momentum, heat, and water vapor are crucial climate data records because they represent lower boundary conditions on the atmospheric circulation and upper boundary conditions of ocean waves and currents. Global measurements of these fluxes using conventional fixed-station systems are impractical making satellite observations attractive. It is very difficult to measure two crucial parameters: the temperature and humidity of the air near the sea surface. The study's motivation is that external information about the air-sea stratification should improve the retrieval of these parameters. We demonstrate a global capability to classify air-sea stratification based on variations in the sea surface texture of high-resolution radar images. This is possible because the turbulent atmospheric boundary layer develops distinct circulations in different stratification regimes. Perturbation surface winds induced by these coherent structures induce a modulation of the ocean surface roughness that is resolved by orbiting radars. An automatic machine learning algorithm detects the characteristic structures, which we correlated to a standard global data assimilation surface analysis. An important research outcome is the largest all-weather data set of boundary layer coherent structures and the conditions under which they exist. Examination of these data will advance our understanding of fundamental boundary layer processes.

1. Introduction

A defining property of the marine atmospheric boundary layer (MABL) is its stratification at the air-sea interface. Over the ocean, with its relatively smooth, but fluid, surface boundary, and variable horizontal temperature gradients, change in near-surface stratification measurably affect mean MABL flow, turbulence, and the surface layer (SL) turbulent air-sea fluxes of momentum, heat, and water vapor. Stratification in turbulent flows quantifies the relative importance of buoyancy and inertial forces and is proportional to the ratio between buoyant and shear turbulent kinetic energy production (Tritton, 1988). It is often quantified using a dimensionless stability parameter based on the Obukhov length scale L, which is a function of the momentum and buoyancy fluxes in the surface layer (Monin & Obukhov, 1954). It seems reasonable to assign conditions to one of three stability regimes: unstable, near-neutral, or stable. A sign change in L defines an unstable versus stable SL and dictates the use of differing bulk air-sea flux formulas. Bulk flux estimates (e.g., Edson et al., 2013) are employed across a range

of applications including MABL field and numerical studies, wind energy resource assessment, and weather and climate prediction models. Forecast models also typically switch between turbulent and eddy-diffusion/mass flux parameterizations (Edwards et al., 2020; Siebesma et al., 2007) when conditions shift from near-neutral toward unstable. These three states also dictate the varied presence, type, and strength of 0.1–5 km scale coherent structures (CS) embedded in the turbulent BL with examples being roll vortices, and, closed- and open-cell convection (Atkinson & Zhang, 1996).

A recognized earth observing system gap is the lack of sufficiently accurate satellite remote sensing methods needed to retrieve SL near-surface air temperature, T_s, and specific humidity, q_s, over the oceans (National Academies of Sciences, Engineering, and Medicine, 2018; Cronin et al., 2019). These crucial scalar measurements are essential for bulk method estimation of surface layer turbulent heat fluxes and stratification. Any data on SL stratification, or differentiation between states, already serves many purposes. This paper explores the efficacy of routine MABL CS observations to estimate stratification. Santellanes et al. (2021) analyzed data collected over Oklahoma to review and expand on the known ability of ground-based radar and Lidar to resolve differing CS and their variation with thermal and mean flow changes. In marine environments, Young et al. (2000) presented a first satellite attempt to relate CS in unstable stratification to the Obukhov length scale using synthetic aperture radar (SAR) surface ocean imagery. During recent ocean investigations using the global Sentinel-1 SAR satellite data set (Wang et al., 2020; Wang, Tandeo, et al., 2019), our team automated the capability to classify common types of CS in SAR imagery, including roll vortices and small-scale cellular convection. As with Santellanes et al. (2021), a third image class emerged that exhibits no significant CS (null case). This paper explores how these three classes map into differing stratification regimes and relate to geophysical controls over the MABL using an enormous new ocean SAR image database classified over years 2016–2019.

CS are a common MABL feature that can be defined as persistent secondary circulations that are not directly related to the local mean flow gradients. They can significantly affect air-sea coupling because they induce vertical momentum, heat, and moisture transport along pathways within the MABL that are not captured by the standard gradient-flux modeling paradigm. The largest CS scale with the depth of the MABL, $h \sim O(1 \text{ km})$, and their lower branches modulate the surface wind at horizontal scales that are usually small multiples of h. This surface wind modulation at scales between approximately $h/2$ and $3h$ produces the SAR signatures under study here, with numerous past examples (Mourad & Walter, 1996; Sikora et al., 1995, 2011; Vandemark et al., 2001; Wang et al., 2020; Young et al., 2005) showing the direct connection between cm-scale surface wave generation due to CS and their detection by C-band SAR.

Past MABL SAR studies typically focused either on CS observed in unstable (cellular features induced by shallow convection) or near-neutral stratification (wind streaks associated with MABL rolls). Transitions between these two embedded signatures, in space and/or time, follow relative variations between surface layer buoyancy and shear production (BP and SP). BP is the air-sea buoyancy flux, which, using bulk flux input variables, is approximately proportional to $-\left(\frac{g}{T_{v_s}}\right) U_s \left(T_{v_s} - SST_v\right)$, where U_s is the near surface wind speed and SST is the sea surface temperature. The humidity-corrected virtual temperature is $T_{v_s} = T_s \left(1 + 0.61 q_s\right)$ and SST_v assumes the air in contact with the water is saturated. SP is the inner-product of the momentum flux and the mean shear and is proportional to $\frac{U_s^3}{z_s}$, where z_s is a reference height for near-surface measurements. Neutral stratification equates to BP = 0, and shear-induced turbulence dominates under near-neutral conditions for either small positive or negative BP. This is the expected niche for wind streak formation (Etling & Brown, 1993; Foster, 2005). Negative (stable) BP weakens shear-generated turbulence and positive (unstable) BP will reinforce it. As stratification becomes increasingly unstable, BP plays a stronger role and will ultimately dominate the generation of turbulence, leading to cellular convection. An open question is what these new observed CS events can reveal about this interplay between buoyancy and shear within the MABL.

We develop a new satellite MABL stratification state indicator based on SAR image texture observations. We focus on images dominated by cellular convection or wind streak textures that we relate to unstable or near-neutral stratification. We also catalog images absent of MABL-scale signatures that largely coincide with stable stratification. Section 2 describes the data and methods. Section 3 demonstrates that the texture-derived image information maps to reference estimates of stratification states in an average sense, at the MABL process level, and at both global and regional/seasonal scales. Implications are discussed in Section 4.

2. Data Sets and Methods

Satellite data come from the European Space Agency's Sentinel-1A (2014 to present) and S-1B (2016 to present) platforms that operate identical C-band SAR systems. Wave mode (WV) is the default SAR data collection mode over the open ocean and each satellite collects nearly 65,000 high resolution (5 m pixel) small (20 × 20 km) WV images per month. WV images are acquired every 100 km along the flight track alternating between mean incidence angles of 23.8° (WV1) and 36.8° (WV2) 90° to the right of the orbital plane. The satellites are 180° apart in the same sun-synchronous (98° inclination) polar orbit with an 18:00 local time of ascending and 12 day repeat cycle. Most ocean areas are consistently and routinely mapped using WV mode with the exception being the eastern North Atlantic due to other sampling objectives. The 20 km WV image size, 100 km spacing, and polar orbit mean that mid-to-high latitudes are sampled more completely. Even with these caveats, the ocean coverage is nearly global and considered comprehensive in terms of sampled atmosphere-ocean conditions. During 2016–2019, more than five million WV images were processed for this study. As described below and in Supporting Information S1, the results in this paper are based on a subset of approximately 600,000 images.

Wang, Tandeo, et al. (2019) and Wang, Mouche, et al. (2019) provide details on 10 prevalent ocean-, atmosphere-, and ice-related SAR signatures observed in the overall WV data set as well as the development of a convolutional neural network (CmWV) model that calculates a probability of occurrence for each these events for any given image. The phenomenon with the highest probability determines the class for each image. This study focuses on images associated with three MABL-related signatures, these being shallow convective cells (MC), wind-streaks (WS), and scenes showing negligible variability at MABL length scales (NV, labeled as POS in Wang, Tandeo, et al., 2019). Wang et al. (2020) showed that wind streaks induce much stronger atmospheric SAR image contrasts at larger incidence angles. Similar enhanced detectability has been confirmed for the MC and NV classes. Accordingly, this study uses only WV2 data.

Figure 1 shows exemplars. Mottled MC cases (Figure 1b) are associated with upward buoyancy flux and generally lighter wind speeds. Their associated MABL structure is a regular pattern of cellular convection generated by nonlinear convective instabilities whose horizontal length scales are comparable to h. The WS signature (Figure 1c) is expected to occur in slightly unstable but near-neutral stratification and are generated by roll CS. WS align near the MABL wind direction because the nonlinear shear instability that generates the rolls is associated with the cross-wind component of the mean flow (Etling & Brown, 1993; Foster, 2005). The lack of atmospheric features in the NV class (Figure 1d) indicates that neither convective nor roll instabilities are strong enough to generate CS. This is most often associated with stable stratification.

Near-surface streaky features that do not span the boundary layer and have much shorter wavelengths than MABL rolls are common in shear-dominated conditions (e.g., Foster et al., 2006; Young et al., 2002). The image-mean WS wavelength has a skewed distribution (almost lognormal) with a mean of 2.6 km and 5th to 95th percentile range of 1.3–4.6 km. Using the ERA5 h, we find the aspect ratio is distributed lognormally with a mean of 2.94 and 5th to 95th percentile range of 1.13–5.75. These wavelength and aspect ratio distributions are consistent with MABL-spanning rolls (Etling & Brown, 1993; Young et al., 2002). Internal waves would have wavelengths at the upper end of this range, but orientations roughly perpendicular to the surface wind. However, the WS orientation and ERA5 surface wind direction always follow each closely with a SD of 22°; which is again consistent with MABL rolls. These characteristics confirm our identification of the WS texture pattern as MABL rolls.

One measure of MABL surface layer stratification is a bulk Richardson number:

$$Ri = \frac{g}{T_{10v}} \frac{z_{10}\,(T_{10v} - SST_v)}{U_{10}^{N^2}} \tag{1}$$

where g is the acceleration due to gravity, U_{10}^{N} is the neutral-equivalent wind speed at $z_{10} = 10$ m above the sea surface and T_{10v} is the virtual temperature at z_{10}. We use U_{10}^{N} because it is the standard remote sensing wind product.

To estimate Ri, we interpolate hourly surface analyses from the European Center Medium-range Weather Forecast (ECMWF) Reanalysis version 5 (ERA5) (Hersbach et al., 2020), adjusted to 10 m, for each WV image. While ERA5 represents an optimized estimate of the surface conditions consistent with available in situ and satellite data, it is understood that both random and systematic error in this chosen reference is expected. However, it is
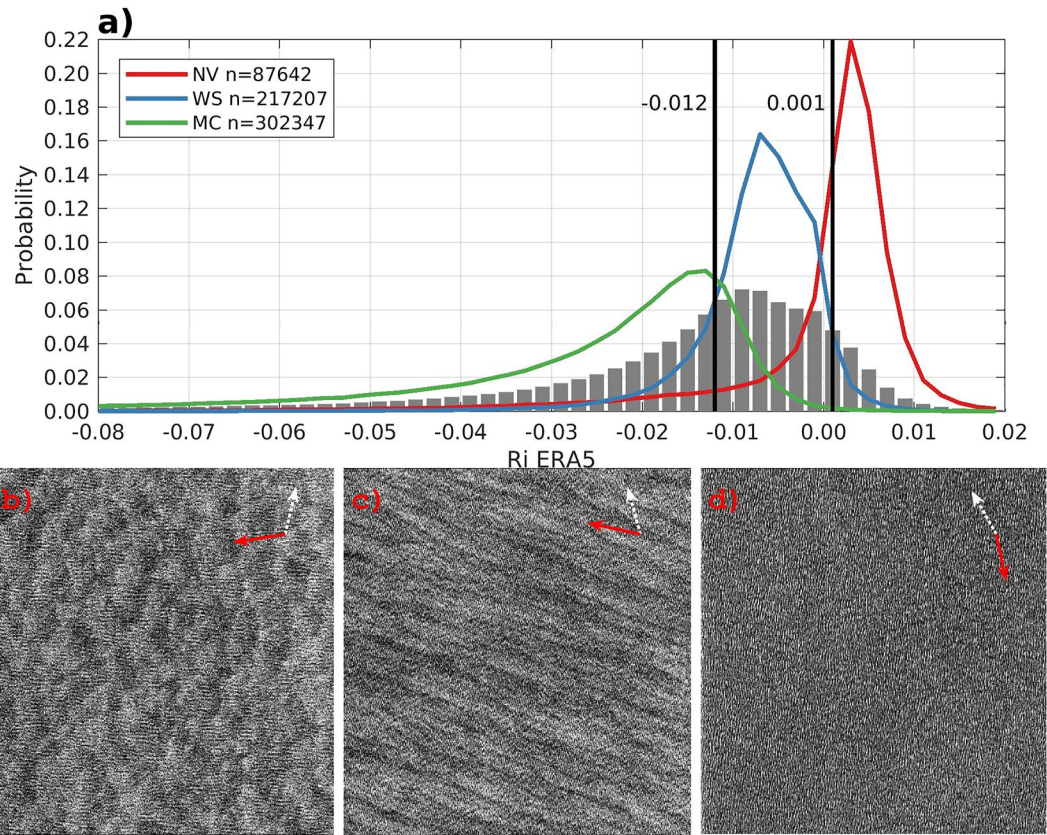
Figure 1. (a) PDFs of MABL Ri estimated from ERA5 for cells (unstable), streaks (near stable), and negligible atmospheric variability (stable) detection from SAR. The shaded gray PDF denotes the entire WV2 population. Representative SAR images for (b) unstable $Ri = -0.032$, $U_{10}^N = 5.3$ ms^{-1}, $\Delta T_v = -2.81°$, (c) near-neutral $Ri = -0.006$, $U_{10}^N = 9.8$ ms^{-1}, $\Delta T_v = -1.74°$, and (d) stable $Ri = 0.005$, $U_{10}^N = 7.6$ ms^{-1}, $\Delta T_v = 0.84°$ MABL states. The white dashed arrow points north and the red solid arrow is the ERA5 wind direction.

assumed that the large data volume will permit development of mean relationships between SAR image classes and Ri. We confirmed the Grachev and Fairall (1997) result that $\frac{z_{10}}{L} \sim 10\,Ri$.

The study uses 4 years of S-1A (2016–2019) and 3 years of S-1B (2017–2019) WV2 images. To ensure robust results, we set a 95% threshold on the MC, WS, and NV classifications. We further required $U_{10}^N \geq 3\,ms^{-1}$, which is near the threshold for wind-wave generation. These criteria results in a data set of 607,196 MC, WS, and NV images. If the threshold is lowered to 50%, the number exceeds 1 million (see Supporting Information S1). Despite our conservative selection criteria, the results are largely insensitive to CmWV threshold. The Supporting Information S1 provides an corresponding set of figures using a CmWV threshold of 50%, which is based on approximately 1 million images.

An important study caveat is that while the CmWV model has a low false alarm rate for MC, WS or NV (especially after a MABL variance threshold is applied to NV; see Supporting Information S1) it is documented that a significant fraction of MC, WS, and NV events go undetected (Wang et al., 2020; Wang, Tandeo, et al., 2019). Therefore, we cannot produce absolute probability maps for the three study classes. Maps shown in the paper reflect relative variations among classes with this caveat.

3. Results

The overall probability distribution function (PDF) of collocated Ri for all WV is shown as the grey bars in Figure 1a. This PDF is very close to the PDF that would have been obtained when combining only the selected MC, WS, and NV data. WS signatures nearly always fall into a relatively narrow range of $-0.02 < Ri < +0.005$ that corresponds to the peak in the overall Ri PDF. The WS inter-quartile range (IQR) is $-0.011 < Ri < -0.003$,
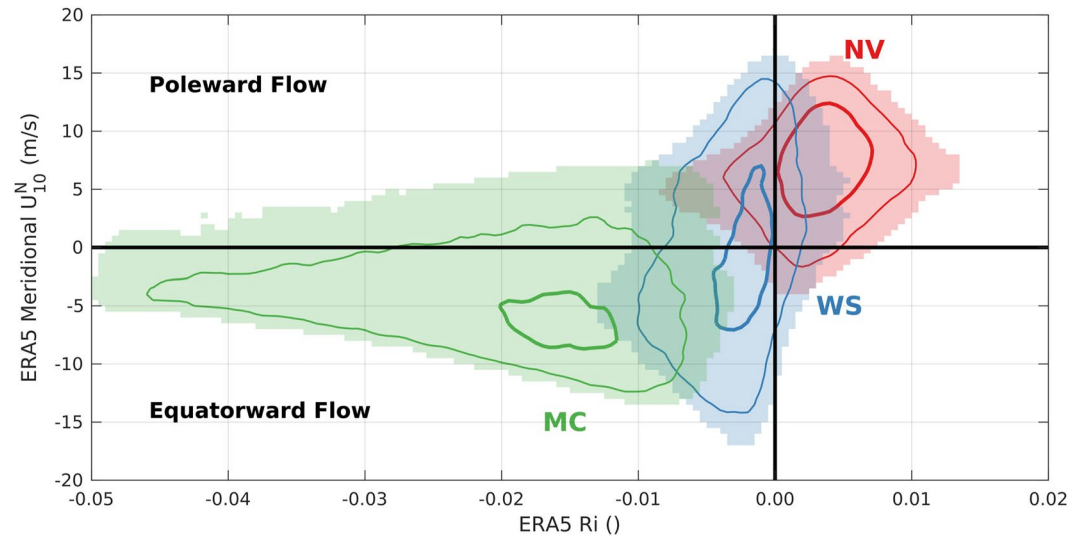
Figure 2. Occurrence of the Ri versus meridional (N–S) wind speed $\left(\mathbf{U}_{10}^{N}\right)$ for the three SAR classes for latitudes greater than $25°N/S$. The green, blue, and red shading represents 10% of the maximum bin within this Ri-U_{10}^{N} space for MC, WS, and NV classes respectively. The thin and thick contours represent 75% and 25% of the population lies inside the lines, respectively.

which is near-neutral unstable stratification. When CmWV detects MC (approximately 50% of the selected images) the PDF of Ri shows that the values are negative and are generally more unstable than the overall distribution with an IQR of $-0.035 < Ri < -0.013$.

With a median Ri of $+0.0026$ and 72% of the images occurring in positive, stable stratification, NV cases occur most often in conditions that are more stable than WS. This makes sense because stable stratification precludes MC and also tends to inhibit WS. A more detailed look at the fewer unstably stratified NV cases shows that both the SP and BP are much lower than typical values for either WS or MC. The presumption is that these NV events are subcritical for the formation of either WS or MC.

If we randomly select WV images using Ri, the textures map into well-defined regimes. When $Ri < -0.02$, the MC texture (Figure 1b) dominates. In the range $-0.02 < Ri < -0.01$, the images textures are a visual mixture of the MC and WS signatures seen in Figures 1b and 1c. When $-0.01 < Ri < 0.001$, the images transition to pure streaks. When Ri is sufficiently positive from ERA5 the SAR image texture has no MABL-scale variability. Based on PDF results in Figure 1a, we define implicit CS bands: (a) Unstable boundary layer (UBL) $Ri < -0.012$, (b) near-neutral boundary layer (NNBL) $-0.012 \leq Ri < 0.001$, and (c) stable boundary layer (SBL) $Ri \geq 0.001$.

Transitions between WV classes can be traced to known MABL modification processes. For example, the mean flow in the mid-latitudes (strong westerly winds and small ΔT_v) results in slightly unstable stratification. The zonal flow is perturbed by baroclinic systems that establish regions of warm and cold thermal advection. Cold advection decreases the local air temperature and tends to make Ri more unstable, while warm advection makes the stratification less unstable and can even turn it positive. Warm advection is mostly associated with poleward flow and cold advection with equatorward flow.

This effect leaves imprints in WV images and is illustrated in Figure 2, which combines data from both hemispheres poleward of 25° latitude to show the distribution of Ri versus the meridional component of $\mathbf{U}_{10}^{N}$ for each of MC, WS and NV. More than 79% of MC observations coincide with equatorward flow, which suggests that cold advection is needed to shift the mid-latitude BL from a NNBL to UBL. In contrast, the NV cases are almost all associated with relatively strong poleward flow. The implication is that warm advection is necessary to establish a SBL. The WS observations sit in between these cases with no clear preference between poleward or equatorward flow. However, nearly all the WS events with $Ri > 0$ coincide with mid-latitude warm advection. There is also a relatively sharp transition from WS to NV.

The full set of observations is mapped in Figure 3 to show where these three signatures are detected and their spatial correlation with Ri. Panels (a–c) show the relative occurrence rate of MC, WS, and NV events. The total
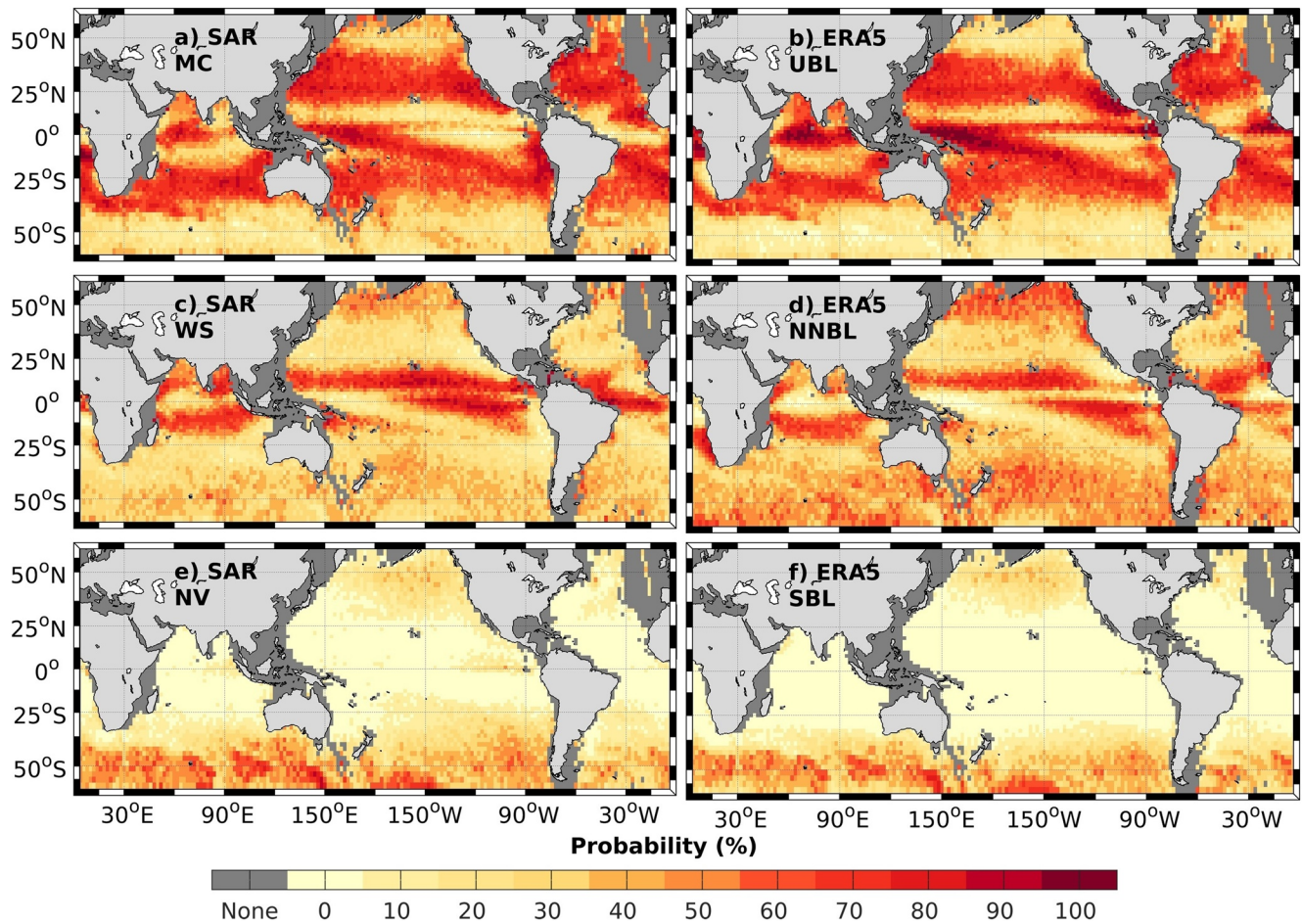
Figure 3. Relative occurrence rate between SAR-detected MC, WS, and NV events, top panels (a–c), using selected 2016–2019 S-1 data. Results are calculated for 2° bins. Panels d–f show the same events but mapped using ERA5 unstable, near-neutral, and stable boundary layer stratification classes based on *Ri* as defined in the text.

across the three classes in any 2° spatial bin adds up to 100%. Similarly and independently, the relative occurrence rates between the three ERA5-defined *Ri* regimes defined above are shown in Figures 3d–3f.

Considering first the SAR data in Figures 3a–3c, recall that: (a) this representation enfolds all seasons over 4 years; (b) S-1 time and space sampling is not synoptic; and, (c) our data set does not yet fully account for all occurences of the three classes. Still, this compilation represents a huge increase in the amount of MABL turbulence cases mapped, both in terms of volume and in providing data over most of the global oceans (c.f. Levy et al., 1999; Sikora et al., 2011).

The most striking features in Figures 3a–3c are the strong inverse presence of WS with MC in the tropics of all oceans, and similarly between MC and NV at mid to high latitudes across the N. Pacific and Southern Ocean. WS dominate the trade wind regions, but the adjoining areas quickly transition to areas dominated by MC just poleward of the trade wind bands (e.g., eastern Tropical Pacific). Note also a stark narrow zonal band of higher MC cases located just north of the equator across the eastern N. Pacific that roughly coincides with the North Equatorial counter current (e.g., Johnson et al., 2002). In the Southern Ocean, there is a near absence of MC cases (<10%). Instead S-1 mostly detects NV and WS. The NV class stands out as having very low population anywhere equatorward of the extra-tropics. Including all seasons, the MC class dominates the subtropical region of all oceans with occurrence rates of 30%–70%. A seasonal breakdown of these divisions is provided in the SI and they do appear to capture expected seasonal transitions in several basins. This finding is revisited in Figure 4.

Turning to Figures 3d–3f and the occurrence rates between *Ri* regimes, the results show remarkably similar spatial variation when compared to the corresponding SAR-detected results, and this for any ocean basin. As
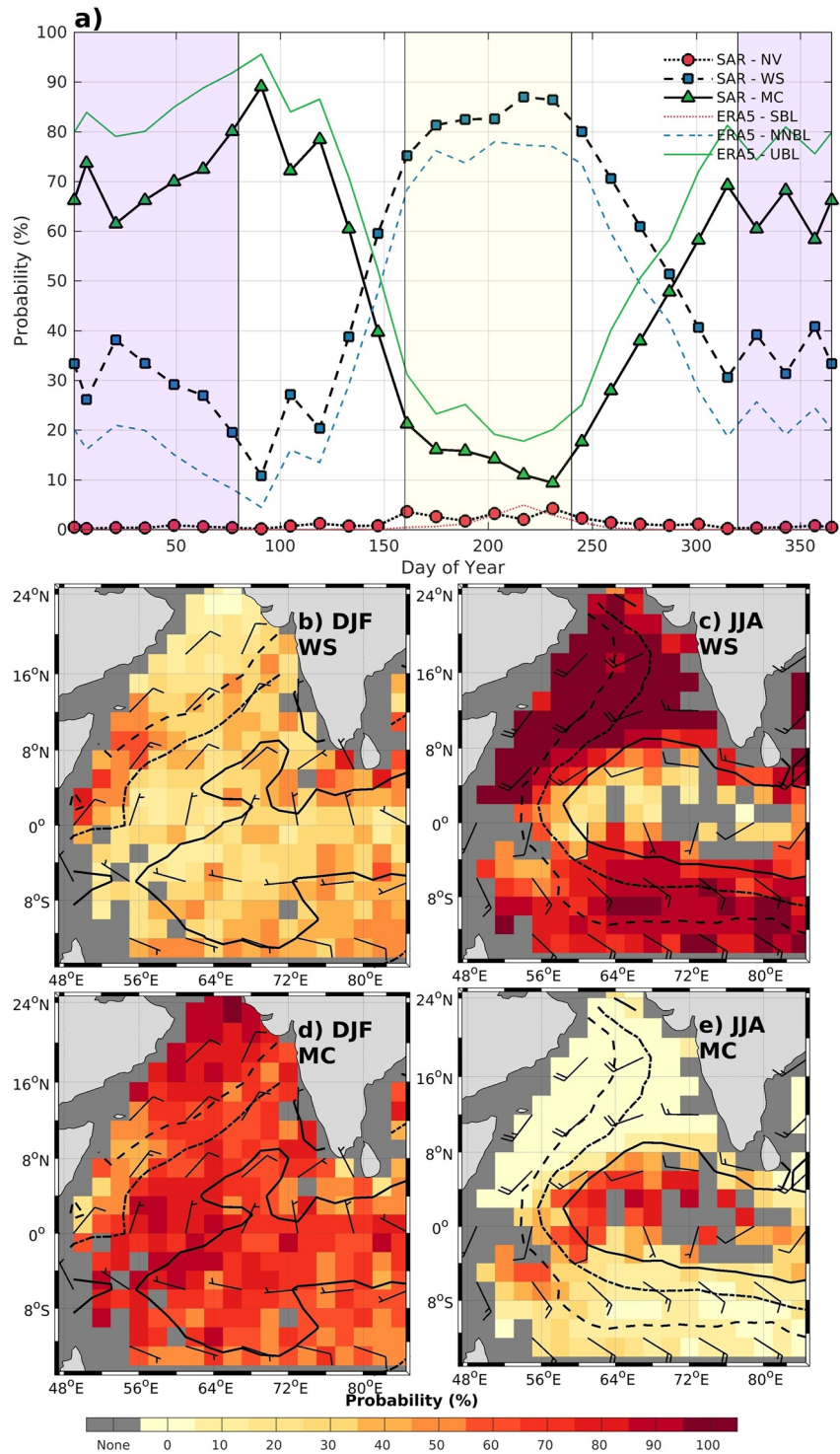
Figure 4. Relative occurrence rates between SAR-detected MC and WS images in the western Indian Ocean. Panel (a) gives the biweekly regional averages. It also shows time series of averages among the three study BL stratification classes using ERA5 *Ri* data. The maps in 2° bin-averaged seasonal WC and MC rates from December–February (DJF) and June–August (JJA) monsoon periods. The surface wind vectors are given as the barbs (direction from) where a full barb is 10 knots. The SST_v 27, 28, and 29°C contours are given as the dotted lines, dash-dot, and solid, lines. These wind and SST_v information are obtained by averaging ERA5 over our larger overall WV2 data set and not the 27% of selected images to show the climatology.

just one example, note the strong Southern Ocean agreement between high stable boundary layer occurrence rate regions for the ERA5 SBL and S-1 NV cases. This is the spatial representation of the MABL modification process associated with warm advection that was discussed in Figure 2. One basin-scale feature that differs between ERA5 and the SAR is the narrow equatorial N. Pacific band mentioned earlier where ERA5 predicts a much higher occurrence of unstable conditions (e.g., UBL > 90% vs. SAR MC > 50% at 5°N, 140°W) and conversely lower occurrence of near-neutral stratification.

Varying the selected Ri boundaries between ERA5 stratification states does not substantially change the regional patterns shown in Figure 3 or their agreement with the SAR data; it only changes the relative occurrence among the three regimes (see Supporting Information S1). A main conclusion drawn from this qualitative assessment is that the measured regional distribution of these three distinct BL signatures (MC, WS, NV), are highly correlated with their corresponding ERA5-classified stratification regime.

The Arabian Sea and western tropical Indian Ocean region has a unique climate dominated by a biannual wind reversal between the winter (October–February) and summer (May–September) monsoon seasons (Schott et al., 2009) that provides a finer-scale view of the space and time information in the WV data set (Figure 4). The bi-weekly average of SAR-detected BL class relative occurrence (Figure 4a) shows an inverted seasonal cycle between MC and WS cases and a very low number of NV events. The similarly averaged ERA5 stratification estimates show a corresponding contrast between the UBL and NNBL stratification regimes (Figure 4a). In the winter monsoon season, WV is dominated by MC (UBL) with 60%–80% occurrence. During the summer monsoon, days 150–240, the pattern reverses and the WS (NNBL) cases dominate with 75%–85% of the observed events. Given the known regional monsoon winds, MC/UBL dominance corresponds with the continental north-east winds of the winter monsoon while the summer period WS/NNBL coincides with southwest winds over the Arabian Sea.

The MC and WS relative occurrence maps shown in Figures 4b–4e for the respective monsoon periods affirm that this strong shift between seasons is observed nearly region-wide. The regional contrasts between MC and WS are most stark in the summer (JJA) monsoon where the WS cases are dominant across the Arabian Sea with more than 90% of the captured events north of 8°N being WS (NNBL) cases, reaching nearly 100% in the central Arabian Sea. Another prominent summer monsoon feature is the local dominance of MC events extending from southern India west to the equator, effectively spanning the Arabian Sea warm pool (Rao et al., 2015). One can also see the light but equatorward winds within this higher JJA MC band that bring cooler air into this area with the warmest regional water, SST > 28°. The winter (DJF) monsoon period differences between the SAR-detected MC and WS events is more uniform across this basin with MC events occurring twice as often as WS events. The largest MC occurrence rates are seen closest to land in the north and southwest (23°N, 64°E; and 06°S, 50°E). The winter monsoon WS cases seldom exceed 35%–40% and do so only near the Somalian current and near southern India. The shift from MC to WS is consistent with the significant increase in the mean regional wind speed between winter and summer monsoon periods seen in Figures 4b–4e. In Supporting Information S1, we show the high regional correlation between these MC and WS data and the respective relative rate mapping of UBL and NNBL for these same seasons.

4. Discussion and Conclusions

The core finding is that there is a fairly strict partitioning of these SAR-observed MABL signatures (MC, WS, NV) into separate surface layer stratification ranges. The composite of more than 600,000 SAR images from all oceans (Figure 1) shows that more than 81% of MC cases occur for $Ri < -0.012$, WS reside in a narrow slightly negative band centered on $Ri = -0.0064$, and ~72% of the NV events occur when $Ri > 0$, that is, demonstrating a new capability to detect $\Delta T_v > 0$. MC and WS are well-defined by SAR-inferred turbulent surface wind patterns that are associated with distinctly different MABL CS. The separation of MABL CS into stratification ranges holds at the MABL process level (Figure 2), in the global averages (Figure 3) and at the seasonal/regional scale (Figure 4) as demonstrated by the shift between MC and WS events with monsoon reversal in the Arabian Sea. Even though Figures 3 and 4 results are not true climatologies, the key point to take from the spatial mapping is that our conservatively selected subset of WV images already provides substantial coverage in space and time and across the typical range of open ocean Ri. Together, the three-regime detection suggests a new observational product for estimating stratification from space.

These new findings greatly improve our understanding of the conditions associated with formation and/or suppression of boundary layer CS and greatly expands upon earlier relevant works that were based on more limited ocean SAR data (Levy, 2001; Sikora et al., 2011; Sikora & Thompson, 2002; Young et al., 2000). That said, large eddy simulation studies (Salesky et al., 2016), recent (Banghoff et al., 2019; Santellanes et al., 2021), and past conventional observations (e.g., Atkinson & Zhang, 1996; Brümmer et al., 1985; Grossman, 1982; Weckwerth et al., 1997) that were collected over land, inland, and open waters are found to be consistent with these new WV results. For example, Weckwerth et al. (1997); Weckwerth et al. (1999); suggested that rolls form at or above $\frac{h}{L}$ of −25 to −15, which corresponds to our MC to WS transition region near $Ri = -0.02$. The SARs ability to detect negligible MABL-scale surface wind variability (NV) is expected to be related to stable surface layer conditions. The NV cases are different than the null cases in land-based radar data of Banghoff et al. (2019) and Santellanes et al. (2021) who define them as having negligible organization, large vertical wind variability, and convection.

The results also have important implications for boundary layer parameterization in numerical models. For example, Figure 2 results imply that CS take quite different forms, or are suppressed, in the different sectors of mid-latitude storms. This presents a serious challenge since CS associated with MC and WS both induce significant non-local turbulent fluxes across the boundary layer that are not captured by purely eddy diffusion modeling paradigm. Some parameterizations, (e.g., Siebesma et al., 2007), add a mass flux transport model to account for convective fluxes. Other parameterizations of convective contributions to the fluxes include Beljaars (1995) and Redelsperger et al. (2000). Roll induced fluxes are more challenging to parameterize (e.g., Glendening, 1996; Zhu, 2008). Development and improvement of parameterizations that include the nongradient fluxes will require a solid observational baseline of occurrence/nonoccurrence of MC and WS.

Rolls are associated with nonlinear shear instabilities that are reinforced by buoyancy, but only over a narrow range of $Ri < 0$ before convective instabilities dominate (Etling & Brown, 1993). Stable Ri is rare in the MABL (dominated by mid-latitude warm advection) and the transition from WS to NV is relatively sharp at small positive Ri. Over land these slightly stable conditions are likely to be even more rare. All of these complications may have led to the common, but misleading, description "horizontal convective rolls." We confirm the theoretical prediction (Brown, 1972) that rolls can persist into the slightly stable regime (approximately 10 k events; Figures 1 and 2) when they are strong enough to maintain an overturning circulation against negative buoyancy flux. A major difficulty in relating surface layer Ri to CS is that while BP is directly related to convection (MC), SL SP is only indirectly related to WS since the nonlinear roll instability depends on the mean shear and stratification profiles. The lack of routine observations of wind, temperature, and humidity profiles in the MABL limits the capability for a more complete analysis. Hence, Ri, or even $\frac{h}{L}$, is likely to be a better predictor of MC than it is for WS. Such details could not be addressed prior to routine WV observations.

A motivation for this study was to improve remote sensing capability for surface flux data records. The expectation is that new and independent sea surface stratification estimates will help constrain T_s and q_s retrievals. Additional benefits to flux products should be possible with the likely prospect that U_{10}^{N} can be retrieved directly from the WV images. Moreover, WV provides a large sampling of each CS/stability regime for comparison to other relevant datasets, measurements concerned with air-sea fluxes, or boundary layer thermal state characterization. The WV CS observations can constrain models and possibly be assimilated into forecast models.

This study broadens the scope of MABL science questions that may be addressed by the new S-1 WV mode data. WV provides global sampling, precise SAR backscatter measurements and a several orders of magnitude increase in MABL CS observations that can be used to address long-standing gaps in our understanding of coherent structures in the boundary layer. Continuing work in each of these areas will require better automated image detection to improve: (a) detection of weaker or misidentified image features and (b) the ability to correctly categorize the transition regime where MC and WS coexist and the transition between WS and NV in slightly stable to stable stratification. This study demonstrates the nearly untapped value of routine WV images to detect the state of the MABL globally and in all weather conditions. Continued examination of these data will advance our understanding of fundamental atmospheric boundary layer processes.

Data Availability Statement

All SAR Wave Mode images are freely available at ESA's Sentinel Open Access Hub (https://sentinel.esa.int/web/sentinel/sentinel-data-access) and also the Alaska Satellite Facility (https://asf.alaska.edu/data-sets/sentinel-1/sentinel-1-data-and-imagery/). The near-surface parameters from the ERA5 data set are available through the Copernicus system (https://doi.org/10.24381/cds.adbb2d47). The model used to classify the Sentinel-1 images is described by Wang, Tandeo, et al. (2019) (https://doi.org/10.1016/j.rse.2019.111457) and trained on the data set that are available at https://doi.org/10.1002/gdj3.73. All data used in this study are compiled into a single netcdf file, deposited into data archive from the open science framework, and it is available here: https://doi.org/10.17605/OSF.IO/9NSGF.

References

Atkinson, B. W., & Zhang, J. W. (1996). Mesoscale shallow convection in the atmosphere. *Reviews of Geophysics*, *34*(4), 403–431. https://doi.org/10.1029/96rg02623

Banghoff, J. R., Sorber, J. D., Stensrud, D. J., Young, G. S., & Kumjian, M. R. (2019). A 10-year warm-season climatology of horizontal convective rolls and cellular convection in central Oklahoma. *Monthly Weather Review*, *148*(1), 21–42. https://doi.org/10.1175/mwr-d-19-0136.1

Beljaars, A. C. M. (1995). The parametrization of surface fluxes in large-scale models under free convection. *Quarterly Journal of the Royal Meteorological Society*, *121*(522), 255–270. https://doi.org/10.1002/qj.49712152203

Brown, R. A. (1972). On the inflection point instability of a stratified Ekman boundary layer. *Journal of the Atmospheric Sciences*, *29*(5), 850–859. https://doi.org/10.1175/1520-0469(1972)029<0850:otipio>2.0.co;2

Brümmer, B., Bakan, S., & Hinzpeter, H. (1985). Kontur: Observations of cloud streets and open cellular structures. *Dynamics of Atmospheres and Oceans*, *9*(3), 281–296. https://doi.org/10.1016/0377-0265(85)90024-7

Cronin, M. F., Gentemann, C. L., Edson, J., Ueki, I., Bourassa, M., Brown, S., et al. (2019). Air-sea fluxes with a focus on heat and momentum. *Frontiers in Marine Science*, *6*. https://doi.org/10.3389/fmars.2019.00430

Edson, J. B., Jampana, V., Weller, R. A., Bigorre, S. P., Plueddemann, A. J., Fairall, C. W., et al. (2013). On the exchange of momentum over the open ocean. *Journal of Physical Oceanography*, *43*(8), 1589–1610. https://doi.org/10.1175/jpo-d-12-0173.1

Edwards, J. M., Beljaars, A. C. M., Holtslag, A. A. M., & Lock, A. P. (2020). Representation of boundary-layer processes in numerical weather prediction and climate models. *Boundary-Layer Meteorology*, *177*(2–3), 511–539. https://doi.org/10.1007/s10546-020-00530-z

Etling, D., & Brown, R. A. (1993). Roll vortices in the planetary boundary layer: A review. *Boundary-Layer Meteorology*, *65*(3), 215–248. https://doi.org/10.1007/bf00705527

Foster, R. C. (2005). Why rolls are prevalent in the hurricane boundary layer. *Journal of the Atmospheric Sciences*, *62*(8), 2647–2661. https://doi.org/10.1175/jas3475.1

Foster, R. C., Vianey, F., Drobinski, P., & Carlotti, P. (2006). Near-surface coherent structures and the vertical momentum flux in a large-eddy simulation of the neutrally-stratified boundary layer. *Boundary-Layer Meteorology*, *120*(2), 229–255. https://doi.org/10.1007/s10546-006-9054-8

Glendening, J. W. (1996). Lineal eddy features under strong shear conditions. *Journal of the Atmospheric Sciences*, *53*(23), 3430–3449. https://doi.org/10.1175/1520-0469(1996)053<3430:lefuss>2.0.co;2

Grachev, A. A., & Fairall, C. W. (1997). Dependence of the Monin–Obukhov stability parameter on the bulk Richardson number over the ocean. *Journal of Applied Meteorology*, *36*(4), 406–414. https://doi.org/10.1175/1520-0450(1997)036<0406:dotmos>2.0.co;2

Grossman, R. L. (1982). An analysis of vertical velocity spectra obtained in the Bomex fair-weather, trade-wind boundary layer. *Boundary-Layer Meteorology*, *23*(3), 323–357. https://doi.org/10.1007/bf00121120

Hersbach, H., Bell, B., Berrisford, P., Hirahara, S., Horányi, A., Muñoz-Sabater, J., et al. (2020). The Era5 global reanalysis. *Quarterly Journal of the Royal Meteorological Society*, *146*(730), 1999–2049. https://doi.org/10.1002/qj.3803

Johnson, G. C., Sloyan, B. M., Kessler, W. S., & McTaggart, K. E. (2002). Direct measurements of upper ocean currents and water properties across the tropical Pacific during the 1990s. *Progress in Oceanography*, *52*(1), 31–61. https://doi.org/10.1016/s0079-6611(02)00021-6

Levy, G. (2001). Boundary layer roll statistics from SAR. *Geophysical Research Letters*, *28*(10), 1993–1995. https://doi.org/10.1029/2000GL012667

Levy, G., Pu, C., & Sampson, P. D. (1999). Statistical, physical, and computational aspects of massive data analysis and assimilation in atmospheric applications. *Journal of Computational & Graphical Statistics*, *8*(3), 559–574. https://doi.org/10.1080/10618600.1999.10474833

Monin, A. S., & Obukhov, A. M. (1954). Basic laws of turbulent mixing in the atmosphere near the ground. *Trudy - Geologicheskiy Institut, Akademiya Nauk SSSR*, *24*, 163–187.

Mourad, P. D., & Walter, B. A. (1996). Viewing a cold air outbreak using satellite-based synthetic aperture radar and advanced very high resolution radiometer imagery. *Journal of Geophysical Research: Oceans*, *101*(C7), 16391–16400. https://doi.org/10.1029/96jc01123

National Academies of Sciences, Engineering, and Medicine. (2018). *Thriving on our changing planet: A decadal strategy for earth observation from space*. National Academies Press. https://doi.org/10.17226/24938

Rao, R. R., Jitendra, V., GirishKumar, M. S., Ravichandran, M., & Ramakrishna, S. S. V. S. (2015). Interannual variability of the Arabian Sea warm pool: Observations and governing mechanisms. *Climate Dynamics*, *44*(7–8), 2119–2136. https://doi.org/10.1007/s00382-014-2243-0

Redelsperger, J.-L., Guichard, F., & Mondon, S. (2000). A parameterization of mesoscale enhancement of surface fluxes for large-scale models. *Journal of Climate*, *13*(2), 402–421. https://doi.org/10.1175/1520-0442(2000)013<0402:apomeo>2.0.co;2

Salesky, S. T., Chamecki, M., & Bou-Zeid, E. (2016). On the nature of the transition between roll and cellular organization in the convective boundary layer. *Boundary-Layer Meteorology*, *163*(1), 41–68. https://doi.org/10.1007/s10546-016-0220-3

Santellanes, S. R., Young, G. S., Stensrud, D. J., Kumjian, M. R., & Pan, Y. (2021). Environmental conditions associated with horizontal convective rolls, cellular convection, and no organized circulations. *Monthly Weather Review*, *149*(5), 1305–1316. https://doi.org/10.1175/mwr-d-20-0207.1

Schott, F. A., Xie, S.-P., & McCreary, J. P. (2009). Indian Ocean circulation and climate variability. *Reviews of Geophysics*, *47*(1). https://doi.org/10.1029/2007rg000245

Siebesma, A. P., Soares, P. M. M., & Teixeira, J. (2007). A combined eddy-diffusivity mass-flux approach for the convective boundary layer. *Journal of the Atmospheric Sciences*, *64*(4), 1230–1248. https://doi.org/10.1175/jas3888.1

Sikora, T. D., & Thompson, D. R. (2002). Air-sea turbulence statistics from synthetic aperture radar: An update. *Canadian Journal of Remote Sensing*, *28*(3), 517–523. https://doi.org/10.5589/m02-037

Sikora, T. D., Young, G. S., Beal, R. C., & Edson, J. B. (1995). Use of spaceborne synthetic aperture radar imagery of the sea surface in detecting the presence and structure of the convective marine atmospheric boundary layer. *Monthly Weather Review*, *123*(12), 3623–3632. https://doi.org/10.1175/1520-0493(1995)123<3623:uossar>2.0.co;2

Sikora, T. D., Young, G. S., Fisher, C. M., & Stepp, M. D. (2011). A synthetic aperture radar–based climatology of open-cell convection over the northeast Pacific Ocean. *Journal of Applied Meteorology and Climatology*, *50*(3), 594–603. https://doi.org/10.1175/2010jamc2624.1

Tritton, D. (1988). *Physical fluid dynamics* (2nd ed.). Oxford University Press, Clarendon Press.

Vandemark, D., Mourad, P. D., Bailey, S. A., Crawford, T. L., Vogel, C. A., Sun, J., & Chapron, B. (2001). Measured changes in ocean surface roughness due to atmospheric boundary layer rolls. *Journal of Geophysical Research: Oceans*, *106*(C3), 4639–4654. https://doi.org/10.1029/1999jc000051

Wang, C., Mouche, A., Tandeo, P., Stopa, J. E., Longépé, N., Erhard, G., et al. (2019). A labelled ocean SAR imagery dataset of ten geophysical phenomena from sentinel-1 wave mode. *Geoscience Data Journal*, *6*(2), 105–115. https://doi.org/10.1002/gdj3.73

Wang, C., Tandeo, P., Mouche, A., Stopa, J. E., Gressani, V., Longepe, N., et al. (2019). Classification of the global sentinel-1 SAR vignettes for ocean surface process studies. *Remote Sensing of Environment*, *234*, 111457. https://doi.org/10.1016/j.rse.2019.111457

Wang, C., Vandemark, D., Mouche, A., Chapron, B., Li, H., & Foster, R. C. (2020). An assessment of marine atmospheric boundary layer roll detection using sentinel-1 SAR data. *Remote Sensing of Environment*, *250*, 112031. https://doi.org/10.1016/j.rse.2020.112031

Weckwerth, T. M., Horst, T. W., & Wilson, J. W. (1999). An observational study of the evolution of horizontal convective rolls. *Monthly Weather Review*, *127*(9), 2160–2179. https://doi.org/10.1175/1520-0493(1999)127<2160:aosote>2.0.co;2

Weckwerth, T. M., Wilson, J. W., Wakimoto, R. M., & Crook, N. A. (1997). Horizontal convective rolls: Determining the environmental conditions supporting their existence and characteristics. *Monthly Weather Review*, *125*(4), 505–526. https://doi.org/10.1175/1520-0493(1997)125<0505:hcrdte>2.0.co;2

Young, G. S., Kristovich, D. A. R., Hjelmfelt, M. R., & Foster, R. C. (2002). Supplement to rolls, streets, waves, and more. *Bulletin of the American Meteorological Society*, *83*(7), 1001. https://doi.org/10.1175/bams-83-7-young

Young, G. S., Sikora, T. D., & Winstead, N. S. (2000). Inferring marine atmospheric boundary layer properties from spectral characteristics of satellite-borne SAR imagery. *Monthly Weather Review*, *128*(5), 1506–1520. https://doi.org/10.1175/1520-0493(2000)128<1506:imablp>2.0.co;2

Young, G. S., Sikora, T. D., & Winstead, N. S. (2005). Use of synthetic aperture radar in finescale surface analysis of synoptic-scale fronts at sea. *Weather and Forecasting*, *20*(3), 311–327. https://doi.org/10.1175/waf853.1

Zhu, P. (2008). Simulation and parameterization of the turbulent transport in the hurricane boundary layer by large eddies. *Journal of Geophysical Research*, *113*(D17). https://doi.org/10.1029/2007jd009643